PNAS RESEARCH ARTICLE | BIOCHEMISTRY

Capturing the native structure of membrane proteins using vesicles

Hang Liu[a], Chun Mong Tse[a], and Shangyu Dang[a,b,1]

Edited by Maofu Liao, SusTech, Shenzhen, China; received November 11, 2024; accepted July 29, 2025 by Editorial Board Member Nieng Yan

Membrane proteins play crucial roles in numerous biological processes and are important drug targets. However, structural studies of membrane proteins often rely on solubilization with detergents, which may not accurately reflect their native states in a cellular context. Additionally, identifying suitable detergents for individual membrane proteins can be a detailed and time-consuming process. Here, we developed a vesicle-based method that preserves the native lipid environment for subsequent structural and functional studies. Using the bacterial multidrug efflux transporter AcrB as an example, we isolated AcrB-containing vesicles and determined its cryo-EM structure with all protomers in a loose (L) state at 3.88 Å by incorporating our micrograph-based sorting strategy. Notably, compared to the L-state AcrB in liposomes and nanoparticles, the exterior transmembrane helices (TMs) in our map exhibited superior quality, featuring a continuous and clear representation of lα, which is positioned horizontally within the lipid bilayer. We further expanded our method by identifying endogenous membrane proteins, including F-ATPase and respiratory complexes, in vesicles generated using mitochondria from pig hearts. The high-resolution structure of respiratory complex III in vesicles revealed a shared subunit nine between two monomers. Briefly, our method presents a promising and straightforward approach for studying the structure and function of membrane proteins in their native environment, eliminating the need for detergent screening and protein purification.

membrane proteins | membrane vesicles | mitochondrial membrane vesicles | in situ structural biology | cryo-EM

Significance

While detergent-based approaches have significantly advanced our understanding of membrane protein structures, they present certain limitations, including resource-intensive detergent screening and the absence of native membrane lipids, which can hinder investigations into lipid-mediated regulation. This has spurred the development of near-native environment strategies such as nanodiscs, Salipro, styrene-maleic acid lipid particles (SMALPs), liposomes, and cell-derived vesicles. Here, we present a vesicle-based method that bypasses traditional purification, preserving native lipids to enable the study of membrane proteins in their cellular environment. With future optimization, this method holds promise for broad application in structural and functional studies of membrane proteins, providing opportunities to capture conformations that reflect their native states.

High-resolution structures provide valuable information to reveal the working mechanism of biological macromolecules. Particularly, membrane proteins, which contribute to more than 60% of drug targets (1, 2), play versatile physiological functions. Since the first atomic-resolution structure of membrane protein was determined in 1985 (3), numerous structures of membrane proteins have been captured (4). These structures not only deepen our understanding of their molecular mechanisms but also facilitate drug development for the treatment of related diseases. Routinely, isolation of membrane proteins from the native cell membrane using detergents is required for subsequent structural and biochemical studies (5, 6). A lot of effort has been spent to obtain well-behaved membrane proteins by screening detergents to solubilize and stabilize the membrane proteins since each protein behaves differently with various detergents (7–9). Although the structures determined by using detergent-solubilized membrane proteins have advanced our understanding in the past decades, the limitations are obvious.

Lipids, important regulators of a majority of membrane proteins (10–12), were not typically included during detergent extraction. Thus, it is incapable of studying the lipid regulatory mechanism using the detergent system. To obtain enough membrane protein suitable for biochemical assays, a lot of effort has been put into detergent screening. For membrane proteins sensitive to local environmental changes, purification may present challenges such as aggregation or unfolding. However, modern mild detergents like glyco-diosgenin (GDN) and lauryl maltose neopentyl glycol (LMNG) often mitigate these issues. Since multiple steps, including affinity chromatography and size exclusion chromatography, are employed in the purification of membrane proteins to ensure high purity of the target protein for subsequent experiments, weakly interacting partners may be lost during these processes, resulting in missed opportunities to study the interaction of the target membrane protein and its binding partners.

In the last decade, several technologies have been developed to study membrane proteins in their native state by mimicking the lipid environment (13). These methods, including nanodiscs (14, 15), Salipro (16), SMALPs (17), proteoliposome systems (18–20), cell-derived membrane vesicles (21), and synaptic vesicles (22, 23). Each method provides unique advantages for structural studies of membrane proteins under various conditions and has significantly contributed to our understanding of biological macromolecules in their native states. Despite their advances, limitations are present. For instance, nanodiscs and proteoliposomes, reconstituted with detergent-purified proteins and commercial

Author affiliations: [a]Division of Life Science, The Hong Kong University of Science and Technology, Clear Water Bay, Hong Kong, China; and [b]The Hong Kong University of Science and Technology-Shenzhen Research Institute, Nanshan, Shenzhen 518057, China

Author contributions: H.L. and S.D. designed research; H.L. and C.M.T. performed research; H.L. and S.D. analyzed data; and H.L. and S.D. wrote the paper.

Competing interest statement: The method using vesicles-based method for structural and functional study of membrane proteins is described in a provisional patent application.

This article is a PNAS Direct Submission. M.L. is a guest editor invited by the Editorial Board.

[1]To whom correspondence may be addressed. Email: sdang@ust.hk.

This article contains supporting information online at https://www.pnas.org/lookup/suppl/doi:10.1073/pnas.2423407122/-/DCSupplemental.

Published September 3, 2025.

lipids, often employ lipid compositions that differ from those found in the native membrane microenvironment where target proteins naturally reside, indicating potential for further optimization.

In this study, we developed a vesicle-based technology to study membrane proteins in their native membrane environment. By bypassing detergent-based isolation and affinity purification of target membrane proteins, this method maximally preserves the native lipid environment and may provide cellular information that has been lacking in previous studies. In addition, this method also saves abundant time and cost by bypassing the tedious optimization of purification, including detergent screening. It has the potential to unravel the mechanism of physiologically important membrane proteins in their native states.

Results

Preparation of Vesicles for Structural Studies. We chose the multidrug efflux transporter acriflavine resistance B (AcrB), a homotrimeric integral membrane protein (24, 25), as an example to test the vesicle-based method. Harvested *Escherichia coli* cells with AcrB overexpressed were treated with lysozyme to break the cell walls (26, 27). In our hands, lysozyme treatment proved essential for obtaining high-quality samples, consistently producing enhanced contrast in negative-stain micrographs. This improvement is likely attributable to the lysozyme-mediated removal of *E. coli* outer membranes and cell walls, a mechanism consistent with prior studies (28–30). The high-pressure homogenizer (French press) was then used to facilitate the formation of vesicles. Unbroken cells and soluble proteins were removed by high-speed and ultraspeed centrifugation. The pellet was resuspended and thoroughly homogenized using the high-pressure homogenizer, and then fractionated by sucrose gradient centrifugation to separate protein-containing vesicles from aggregated ones and other impurities (Fig. 1*A* and *SI Appendix*, Fig. S1).

During vesicle preparation, we observed that the concentration of vesicles is crucial for preparing high-quality cryosamples suitable for cryo-electron microscopy (cryo-EM) studies. Vesicles tend to remain on the carbon film rather than enter the holes of grids (*SI Appendix*, Fig. S1*D*). Although continuous sucrose gradient centrifugation is effective for accurately separating vesicles of varying densities, it requires a longer processing time (typically overnight) and, importantly, results in sample dilution in a large volume (*SI Appendix*, Fig. S1*A*). However, high-fold concentration of vesicles from a large volume to a small volume using Amicon Ultrafiltration Filters necessitates prolonged centrifugation, which can easily lead to vesicles binding to the filter membrane and subsequent aggregation into precipitates. Additionally, traditional strategies for cryogrid preparation of low-concentration samples, such as using continuous carbon grids or multiple loadings, were unsuccessful due to low contrast or thick ice in the final grids.

To address this issue, we optimized the sample preparation protocol by employing a noncontinuous sucrose gradient centrifugation approach. The quality of the vesicle samples was initially assessed using continuous sucrose gradient centrifugation, which also allowed us to determine that the density of the AcrB vesicles corresponds to approximately 30% (w/v) sucrose solution based on the positions of the collected fractions. For large-scale vesicle purification, we then employed a noncontinuous gradient consisting of two layers of 20% and 40% sucrose solutions (*SI Appendix*, Fig. S1*B*). This approach significantly reduced processing time (typically 1 h) and allowed for the rapid concentration of vesicle samples at the interface of the two layers (*SI Appendix*, Fig. S1*C*). The optimized protocol, which combines continuous and noncontinuous sucrose gradient approaches tailored to different needs, enables us to achieve a higher concentration of high-quality vesicles suitable for cryosample preparation.

A clear band on sodium dodecyl-sulfate polyacrylamide gel electrophoresis (SDS-PAGE) representing AcrB indicated successful isolation of vesicles with the target protein (Fig. 1*B*). In comparison to the sample before sucrose gradient centrifugation, the postcentrifugation sample exhibited a clearer background and more homogeneous vesicle sizes, as checked by negative staining EM (Fig. 1 *C* and *D*). Additionally, the majority of the vesicles obtained after sucrose gradient centrifugation were less than 100 nm in size, with many even below 50 nm, making them appropriate for cryo-EM studies (Fig. 1*D*).

Characterization of AcrB Vesicles in Cryo-EM Sample. The high concentration of sucrose introduced significant background noise, hindering high-resolution structure determination using single-particle cryo-EM. To address this issue, the collected vesicles from noncontinuous sucrose gradient centrifugation were diluted and concentrated several times to reduce the sucrose concentration to less than 1%. After buffer exchange, the vesicle samples were directly loaded onto holey carbon grids for cryosample preparation. The cryo-EM micrograph suggested that vesicles range in size from 20 to 200 nm, with the majority (over 50%) approximately 50 nm in size, consistent with the observations from negative staining EM (Fig. 2*A*).

We also investigated vesicle distribution in vitreous ice using cryoelectron tomography (cryo-ET). Outside the grid holes, vesicles tended to attach to the surface of the carbon film, consistent with our observation that most vesicles remained on the carbon film, as shown in the low-magnification micrograph (*SI Appendix*, Figs. S1*D* and S2). Inside the grid holes, vesicles were randomly distributed within an ice layer approximately 120 nm thick, with no discernible preference for the air–water interfaces (AWIs) (*SI Appendix*, Fig. S2 *B* and *C*). This observation indicates that vesicles are nonuniformly distributed in the grid, with a preference for the carbon film. Consequently, a relatively high concentration of vesicles is required to push them into the grid holes during cryosample preparation.

We further reconstructed tomograms to explore the details of vesicles inside the grid holes. Within some vesicles, features of membrane proteins, likely AcrB, were visible, indicating a high density of overexpressed proteins in the bacterial membrane (*SI Appendix*, Fig. S2 *D* and *E*). Interestingly, two types of vesicles, inside-out and inside-in, were observed, distinguished by the orientation of the inserted membrane proteins (*SI Appendix*, Fig. S2*E*). Additionally, we noted a few irregular membrane fragments, possibly derived from damaged vesicles or bacterial cells during the cryosample preparation (*SI Appendix*, Fig. S2*C*).

Both cryo-EM and cryo-ET results suggest that vesicles in grid holes are freely distributed within the vitreous ice, exhibiting favorable behavior and being minimally damaged by the AWIs. This indicates their potential as a promising method for performing structural studies of membrane proteins without the need for purification.

The Micrograph-Based Sorting Approach Enabled High-Resolution Structure Determination of AcrB in Vesicles. Compared to traditionally purified samples, it is more difficult to identify individual protein particles embedded in the vesicle membrane in the cryo-EM micrographs of AcrB in vesicles due to the strong background signals from the vesicle membrane, as previously noted (31, 32). To achieve high resolution, we employed various strategies in a stepwise manner.

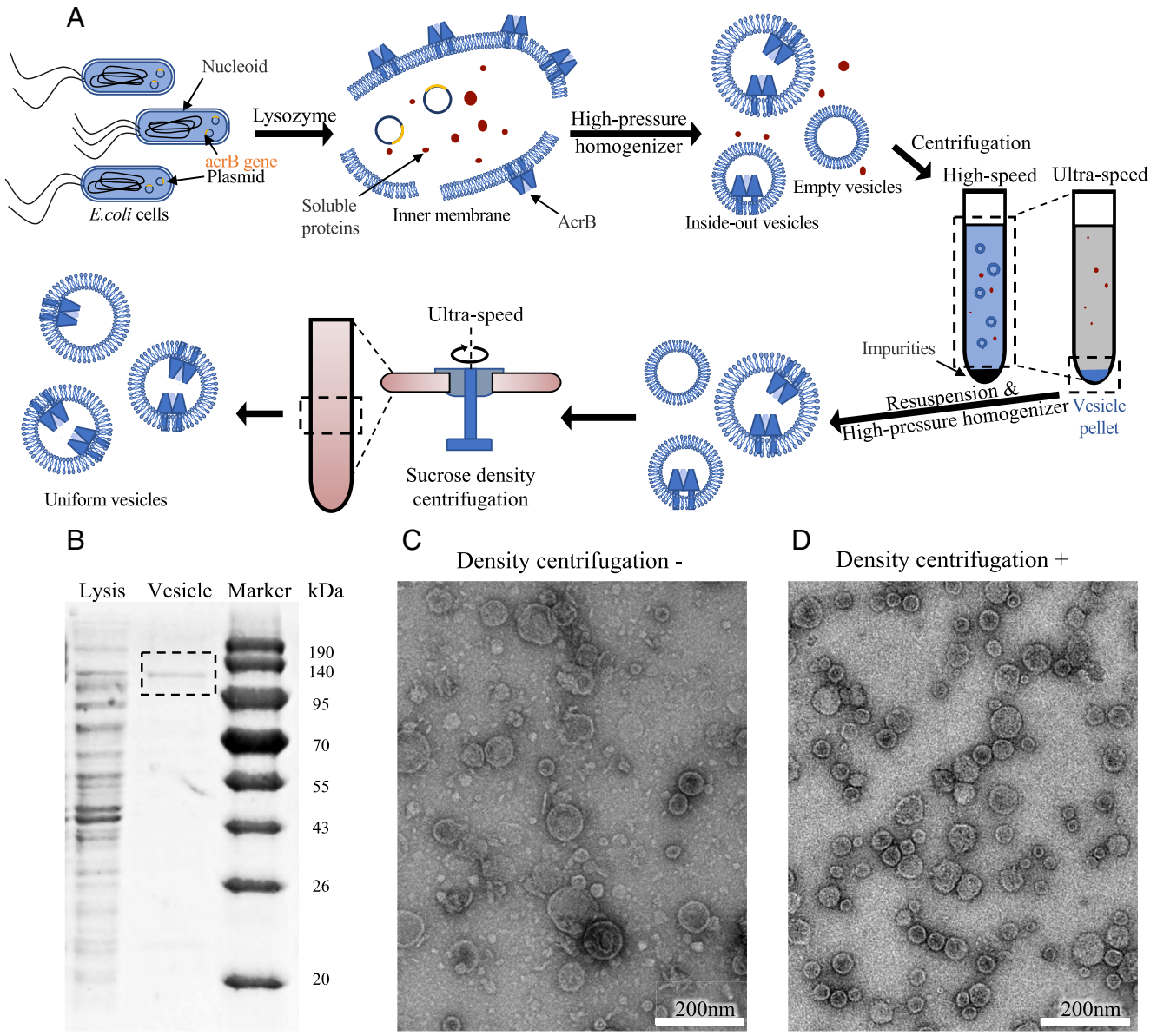

Fig. 1. Generation of vesicles from the *E. coli* cell membrane. (*A*) A workflow for vesicle preparation using AcrB overexpressed bacterial cells. (*B*) SDS-PAGE indicates successful vesicle preparation. Lysis: cell lysate after the high-pressure homogenizer, containing various vesicles and soluble proteins. Vesicle: vesicle sample after high-speed and ultraspeed centrifugation. The target band of AcrB (~110 kDa) is indicated with a black dashed box. (*C*) A representative negative stain image of the vesicle sample without sucrose density centrifugation purification. (*D*) A representative negative stain image of one uniform vesicle fraction after sucrose density centrifugation. Scale bars are indicated in the *Bottom Right* of the images.

The traditional data processing approaches using cryoSPARC (33) only resulted in a medium-resolution map of around 7.5 Å for AcrB in vesicles. Many attempts to improve the resolution were unsuccessful, probably because of the low signal-to-noise ratio (SNR) of the particles, which hindered the effective sorting of top-tier particles from generally good ones and limited further 3D classification and refinement (*SI Appendix*, Fig. S3*A*).

To tackle this problem, we developed a micrograph-based sorting method to classify particles and enhance their quality, combined with deep learning particle picking using Topaz (34, 35) (Fig. 2*C* and *SI Appendix*, Fig. S3 *A–C*). Briefly, micrographs are first grouped into three categories (high, medium, and low) based on the number of particles that contributed to the 7.5-Å cryo-EM map mentioned above. Only micrographs containing a relatively high number of good particles (>20) were selected as input for training the deep learning particle picking model, aiming to improve precision and accuracy. The well-trained model was then used to pick particles from micrographs in the high and medium categories (around 1,068). These particles were extracted for multiple rounds of 2D classification, three-dimensional (3D) classification, and refinement to generate a cryo-EM map with improved resolution of 6.5 Å (Fig. 2*C* and *SI Appendix*, Fig. S3*B*).

The aligned particles used for the generation of 6.5-Å map served as a seed to guide 3D classification of good particles from those picked by Topaz across all micrographs. Particles were further cleaned through 2D and 3D classification, improving resolution to 4.5 Å, which was subsequently enhanced to 4.1 Å by applying CryoSieve (36). This 4.1-Å map was then used as an updated 3D seed to repeat the process, generating a 4-Å map from approximately 50,000 particles. Finally, symmetry expansion, local refinement, and postprocessing were applied to obtain the cryo-EM structure of AcrB in vesicles at 3.88 Å (Fig. 2*C* and *SI Appendix*, Fig. S3*C*).

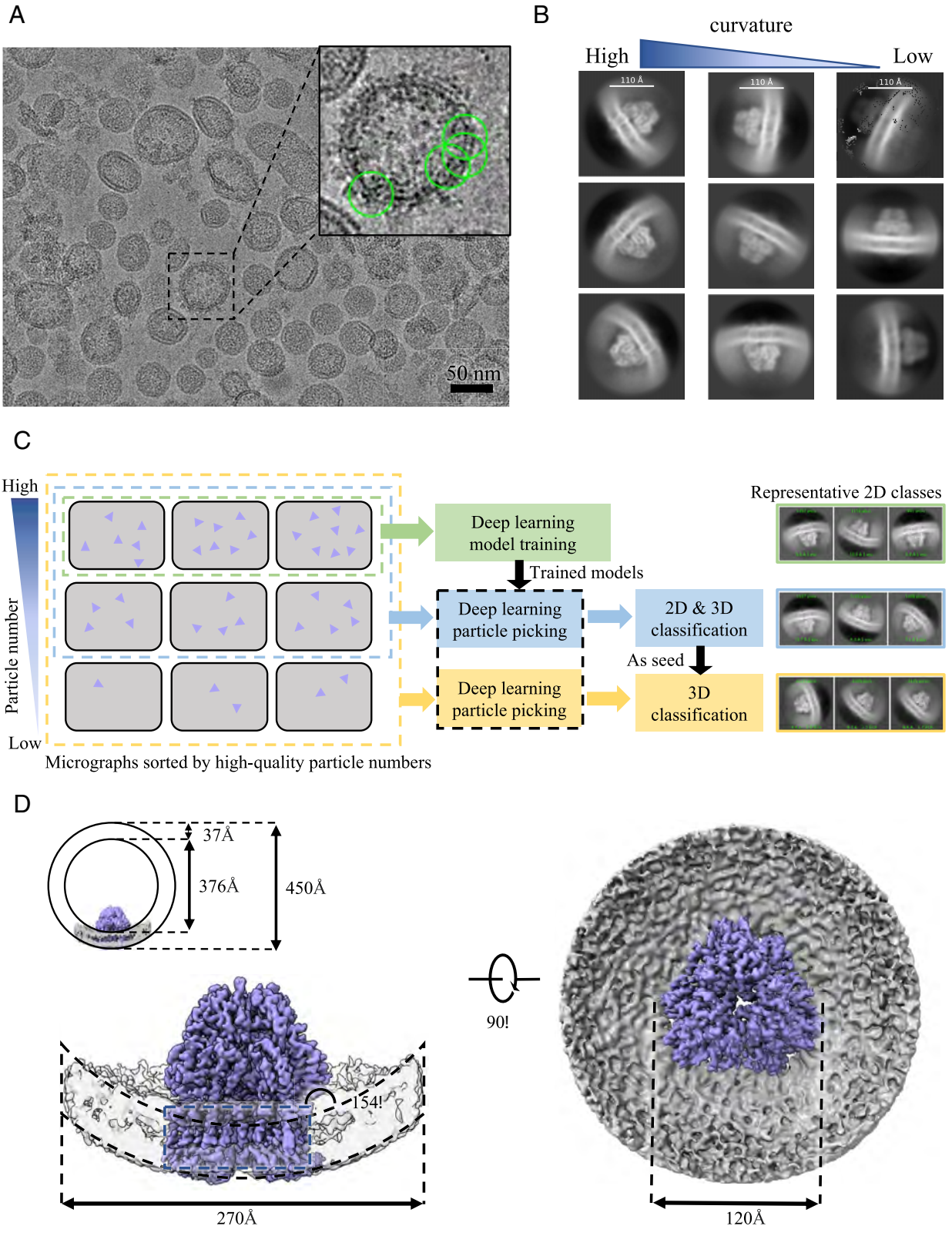

Fig. 2. Cryo-EM structure determination of AcrB in vesicle. (*A*) A representative cryo-EM image of vesicles. A typical vesicle containing AcrB (green circle) is shown in the zoom-in view. (*B*) Representative two-dimensional (2D) class averages with clear AcrB features. The 2D classes also indicate different membrane curvatures. (*C*) The micrograph-based sorting approach used for AcrB particles picking and classification. The representative 2D classification results of every step are shown to evaluate particle quality. (*D*) Side (*Left*) and *Top* (*Right*) views of the cryo-EM density map of AcrB (purple) in the vesicle membrane (gray). The original curvature of the vesicle membrane is indicated by the black dashed lines. The transmembrane region of AcrB is indicated by the blue dashed lines. The average vesicle thickness and size are labeled in the *Upper Left*.

We also identified AcrB particles in top and bottom views through template-based particle picking, which is further supported by cryo-ET observations (*SI Appendix*, Fig. S2*E*). Although the 2D averages of these particles displayed some AcrB-like features, they lacked detail compared to the 2D projections generated from the final reconstructed map (*SI Appendix*, Fig. S4 *A*–*C*).

Combining these top and bottom view particles from reasonable 2D averages did not enhance the final 3D reconstruction, likely due to the challenges in aligning or classifying these particles caused by significant background noise from the vesicles. Therefore, only side-view particles were used for the final reconstruction of AcrB in vesicles.

Furthermore, during data processing, we observed that the membrane density with various curvatures was present in the 2D averages. Further analysis revealed that most AcrB particles were in inside-out vesicles, with only 4.6% belonging to inside-in vesicles (Fig. 2 *A* and *B* and *SI Appendix*, Fig. S4 *D–F*). Interestingly, membrane pieces that failed to form vesicles during sample preparation contributed to 3.7% of final particles, exhibiting a flat membrane density (*SI Appendix*, Fig. S4 *D–F*). This finding is also consistent with our observations in the previously mentioned cryo-ET studies (*SI Appendix*, Fig. S2*C*).

The native membrane surrounding AcrB showed clear curvature in the final 3D reconstruction. Through a rough measurement, the average size of vesicles was around 450 Å in diameter with an estimated membrane thickness of 37 Å, consistent with the observation from raw micrographs (Fig. 2*D*). The curvature of the 120 Å wide membrane transitioned nearly to a flat configuration in the AcrB transmembrane region, forming a 154° angle with the vesicle surface (Fig. 2*D*). This change in curvature is highly consistent with the behavior of AcrB in liposomes, despite the absence of a strict size control method for our vesicles.

The micrograph-based sorting approach we present here may enhance high-quality particle identification by providing a more reliable picking model for Topaz. This, combined with 3D-seed guided classification and CryoSieve, gradually improves resolution and enables the achievement of a high-resolution structure of AcrB in vesicles (Fig. 3 *A–C* and *SI Appendix*, Fig. S3 *D–F* and Table S1). These results demonstrate that it is feasible to obtain high-resolution structures of membrane proteins, such as AcrB, within the native cell membrane by generating vesicles.

Structural Analysis of AcrB in Vesicles. The molecular mechanism of AcrB has been extensively studied. To successfully transport its substrate, AcrB undergoes three major conformational states, which include the loose (L), tight (T), and open (O) states (37). The functional AcrB complex exists in the LTO state as an asymmetric trimer to transport cargo, with each monomer cycling through the three conformations (25). Theoretically, the apo AcrB trimer, without binders, strictly followed the C3 symmetry with all protomers in L states, as shown in the first crystal structure of AcrB, as well as the cryo-EM structure of apo AcrB reconstituted in liposomes (19, 38). Interestingly, the cryo-EM structure of AcrB extracted with SMA from the bacterial membrane was captured in the asymmetric LTO state (39). Furthermore, the structures of apo AcrB crystalized under different buffer conditions were also reported in the asymmetric LTO state previously (40) (Fig. 3*D*). Structural evidence and long-term studies of AcrB's functional models suggest that purified apo AcrB may be dynamic and

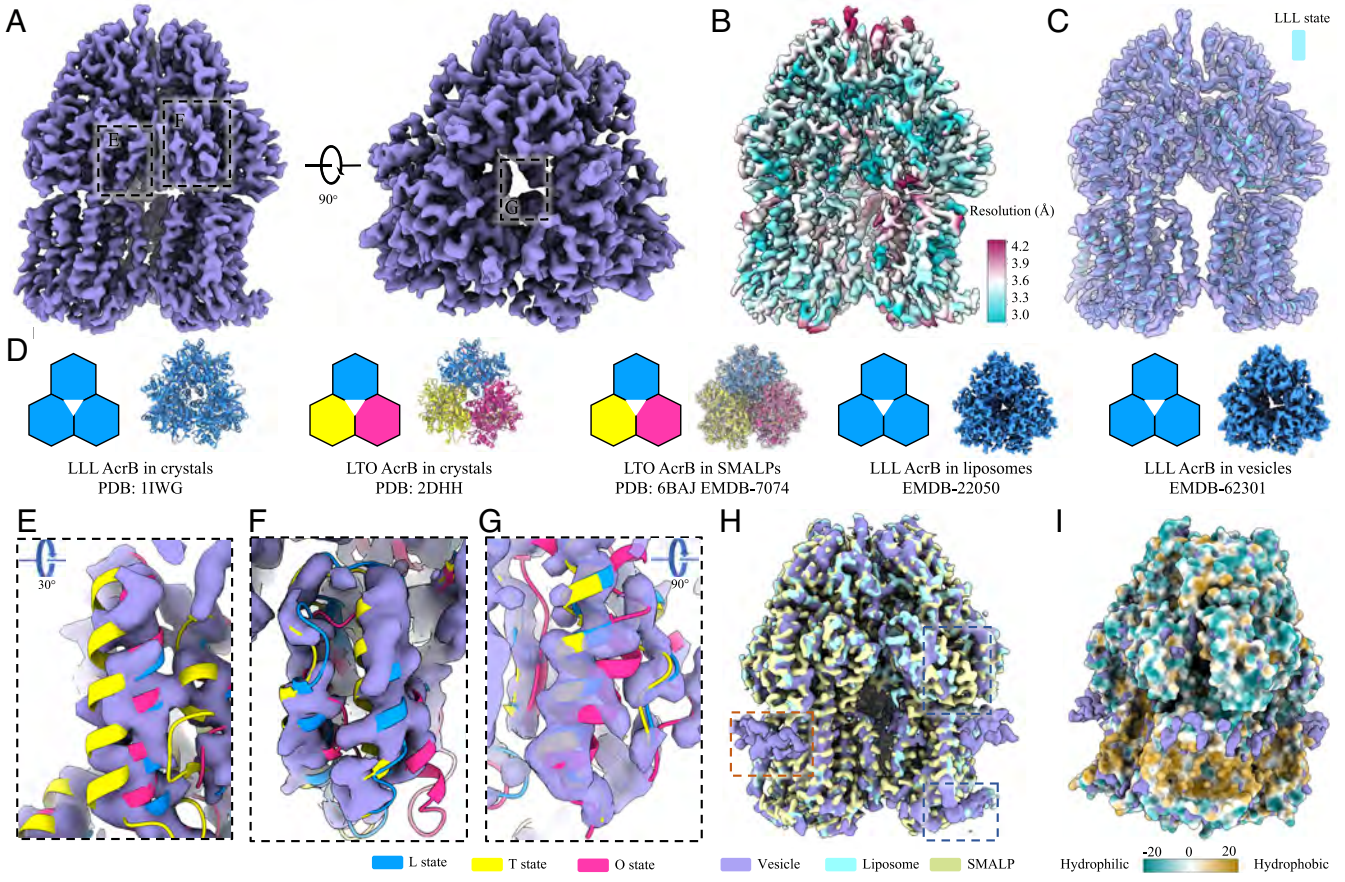

Fig. 3. Structural analysis of AcrB in vesicles. (*A*) The cryo-EM density map of AcrB in vesicles shown from two different views. (*B*) Local resolution estimation of AcrB. (*C*) Superimposition of the cryo-EM density map of AcrB in vesicles with the model in the LLL state (PDB: 1IWG). (*D*) Structures and models of representative AcrB in different functional states. (*E–G*) Superimposition of AcrB structures (PDB: 2DHH) in L (blue), T (yellow), and O (magenta) states with cryo-EM density map of AcrB in vesicles. The positions of these three regions are indicated in (*A*) accordingly. (*H*) Comparison of AcrB maps obtained in vesicles (purple, this study), liposomes (cyan, EMD-22050), and SMALP (brown, EMD-7074). Regions showing differences in protein and lipid are labeled with black boxes and red boxes. (*I*) The molecular lipophilicity potential map of AcrB (PDB: 1IWG) merged with the lipid density from the cryo-EM map of AcrB in vesicles.

flexible. This flexibility may contribute to the lower resolution and the various conformations observed in the structural results of apo AcrB compared to ligand-bound AcrB. Protein–lipid interactions may be a critical factor influencing the stability of AcrB proteins, although scientists still know little about these interactions, particularly in the native membrane environment (41).

To determine whether AcrB in vesicles exhibits distinctive properties, we conducted a structural analysis and compared it with other available structures of AcrB determined under different conditions. The local resolution analysis revealed no significant resolution differences across the various regions of AcrB (Fig. 3*B*). The majority of the regions, including the funnel domain and porter domain on the periplasmic side, as well as several exterior TMs, displayed higher resolutions ranging from 3.0 Å to 3.6 Å, while the periplasmic halves of the two interior TMs (TM5 and TM6) exhibited a relatively lower resolution of approximately 4 Å (Fig. 3*B*). These observations are consistent with a previous study (19), probably due to the dynamic nature of the interior TMs of AcrB in the L state. Additionally, the exterior TMs may be stabilized by the lipid molecules they face, a phenomenon also observed in other membrane proteins, such as TRPV1 reconstituted in nanodiscs (42). Notably, compared to the cryo-EM density maps of L-state AcrB in liposomes and nanoparticles, our cryo-EM density map of the exterior TMs exhibited better quality, featuring a continuous and high-quality representation of lα (43). The lα helix (G511-S537), which connects TM6 and TM7, is positioned horizontally close to the inner membrane. Intriguingly, in our cryo-EM density map, this lα helix is buried in the lipid bilayer (*SI Appendix*, Fig. S5 *A* and *B*). These interesting observations suggest that our gentle preparation method for the vesicles, which avoids the use of additional chemicals and extra purification steps, may help preserve the native membrane environment and stabilize the AcrB transmembrane region through protein–lipid interactions.

To identify the states of AcrB in vesicles, we applied both C3 and C1 symmetry in the final local refinement for our analyses. The comparison of the cryo-EM maps generated with C1 and C3 symmetry showed insignificant conformational changes (*SI Appendix*, Fig. S5*C*). By docking the AcrB monomer atomic models in the L, T, and O states into our cryo-EM maps, we identified three major regions with helix shifts consistent with the conformational changes. Notably, AcrB in vesicles aligned better with the L state than with the other two states across all three regions (Fig. 3 *C* and *E*–*G* and *SI Appendix*, Fig. S5*C*). Our structural analyses indicate that the overexpressed AcrB in vesicles adopts an LLL state, which is highly consistent with the structure obtained from liposomes, while differing from the structure obtained using the SMA extraction method (Fig. 3*H*).

Although the majority of membrane signals were averaged out during focused refinement of the protein region, particularly with C3 symmetry applied, our map revealed additional densities near the membrane surface (Fig. 3*H* and *SI Appendix*, Fig. S2*D*). Molecular lipophilicity potential analysis indicated that these densities likely correspond to the hydrophilic heads of lipids from the bacterial membrane, located on the hydrophilic region of the transmembrane helices of AcrB (Fig. 3*I*). We further compared the densities of nonprotein regions in the final map of AcrB in vesicles with the maps of AcrB obtained from liposomes and nanoparticles (Fig. 3*H*). Intriguingly, the extra densities were unique to our results. We also observed lipid densities in the center of the AcrB C1 map, which were significantly weakened in the C3 map, suggesting that the membrane interior of the trimer may be more fluid rather than tightly bound to the protein (*SI Appendix*, Fig. S5*D*).

These structural analyses further demonstrate that our vesicle-based method can be used to explore the structural details of membrane proteins in their native lipid environment without introducing artifacts. Additionally, the extra lipid densities unique to our map of AcrB in vesicles may be related to its functional properties.

Structure of Respiratory Complexes in Vesicles. To evaluate whether our vesicle-based method could be applied to endogenous membrane proteins and other systems, we purified mitochondria from pig hearts and generated vesicles following a similar protocol. In contrast to vesicles derived from bacterial cell membranes, mitochondrial membrane vesicles exhibited a more irregular and less smooth surface, likely due to their higher membrane protein density and protein-driven membrane curvature changes. Despite some size heterogeneity and minor aggregates from protein denaturation, the samples remained viable for cryo-EM studies (Fig. 4*A*).

To comprehensively explore mitochondrial resident proteins, we randomly picked particles from vesicle membranes without template bias. Iterative 2D classification of these particles yielded several classes exhibiting distinct features of mitochondrial membrane proteins, including F-type adenosine triphosphate (ATP) synthase (F-ATPase, also known as respiratory complex V) and respiratory complex III (CIII) (Fig. 4 *B*–*E*). We then trained deep learning particle-picking models using the micrograph-based sorting approach to specifically enrich for F-ATPase and CIII, respectively (Fig. 4 *C* and *D* and *SI Appendix*, Fig. S6*A*).

The characteristic structural features of F-ATPase, including the stalk, catalytic hexamer, and transmembrane F0 region, were clearly resolved in 2D averages (Fig. 4 *B* and *D*). Notably, the stalk induced membrane bending at a specific angle, consistent with previous reports (44). Dimeric F-ATPases are well documented on inner mitochondrial membranes, although their assembly mechanism and physiological significance in mammalian cells are debated (44–46). Previous studies have also demonstrated that detergent-purified F-ATPase from algae and yeast retains dimeric configurations in liposomes, distorting the membrane and forming rows (46). While several 2D class averages displayed faint paired ATPase signals, these were ultimately attributed to nonspecific particle crowding through trace-back analysis of raw particle images, with no observed instances of native oligomeric arrangements (stalk-to-stalk binding) (Fig. 4 *A* and *D*). Intriguingly, the F-ATPase in our vesicle samples predominantly appeared in monomeric form with no detectable native dimer features, which may be related to the changes in membrane structure and physiological environment during vesicle preparations (Fig. 4*D*). Although 2D averages revealed clear structural features, 3D reconstruction of F-ATPase achieved only medium resolution, comparable to a recent study (47), likely reflecting the intrinsic dynamics of this complex.

In contrast, we successfully identified CIII in vesicles and determined its structure at 3 Å (Fig. 4 *F* and *G* and *SI Appendix*, Fig. S6). Notably, while most structural studies of respiratory chain complexes typically target entire supercomplexes for particle selection (48, 49), our approach initially isolated CIII particles, likely facilitated by its high abundance. Topaz training, together with our micrograph-based sorting approach, enabled remarkable specificity in particle picking to further enrich CIII particles for 3D reconstruction (Fig. 4*C* and *SI Appendix*, Fig. S6 *A* and *B*). Subsequent expansion of the box size allowed for the identification of particles from complexes I (CI) and IV (CIV), as clearly visualized in 2D class averages (Fig. 4*B*). Moreover, 3D classification revealed that only ~35% of CIII participated in supercomplex

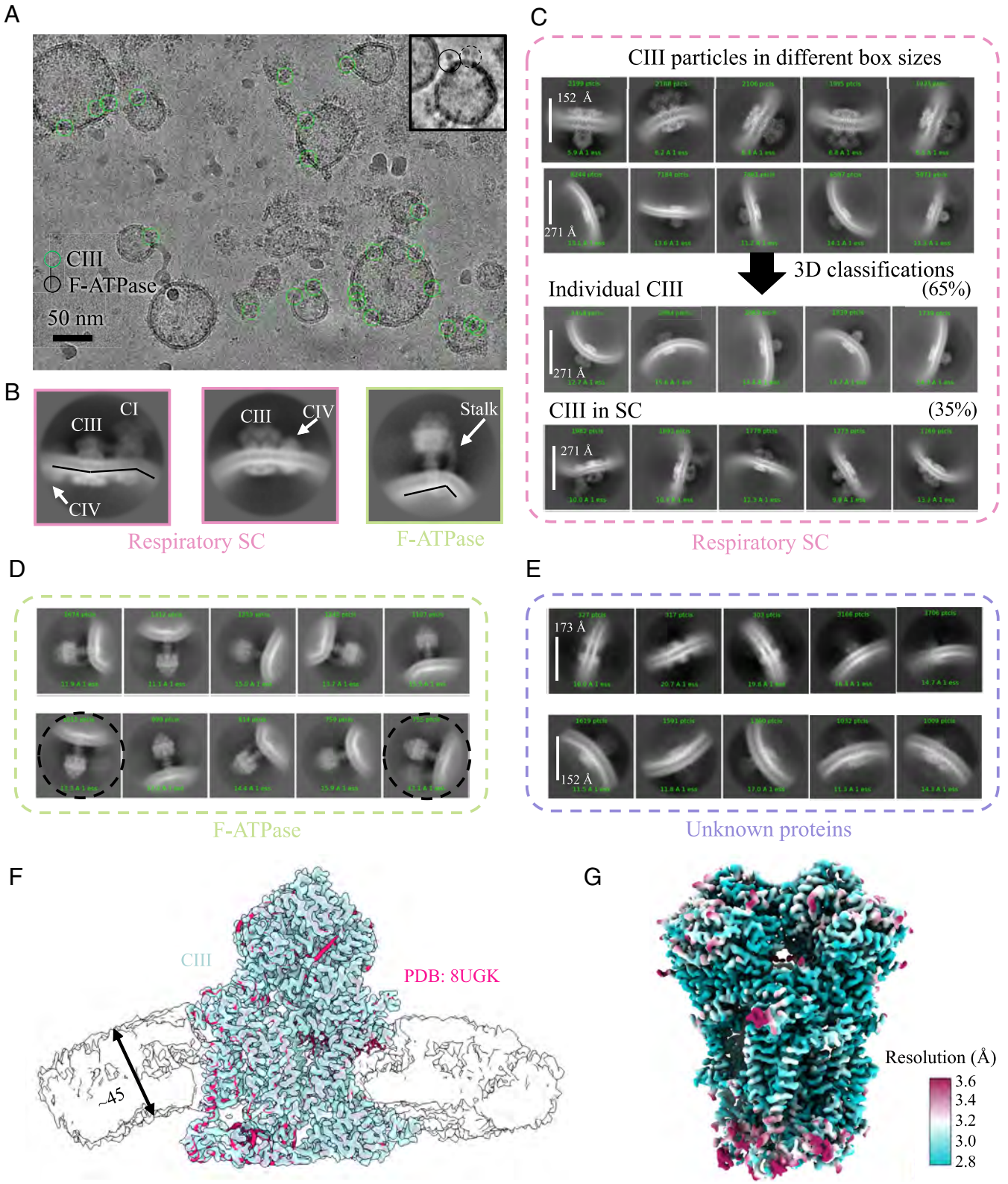

Fig. 4. Cryo-EM structure determination of endogenous mitochondrial membrane proteins using vesicles. (*A*) A representative cryo-EM image of vesicles. CIII and F-ATPase are labeled with green and black circles, respectively. (*B*) Representative 2D average images of the respiratory supercomplex and F-ATPase showing clear details of complex components. (*C*) Representative 2D classification results of CIII in different box sizes (*Top*) and states (*Bottom*). (*D* and *E*) Representative 2D classification results of F-ATPase (*D*) and unknown proteins (*E*). The partial 2D classes showing weak features from the F-ATPase adjacent are labeled with black circles. (*F*) Side view of cryo-EM density map of CIII (cyan) in the vesicle membrane (gray). The atomic model (PDB: 8UGK, red) from the native pig heart mitochondria is superimposed into the map. (*G*) Local resolution estimation of CIII in vesicles.

formation, with the majority (65%) existing as independent particles (Fig. 4*C*). This phenomenon has been previously observed in detergent-purified respiratory supercomplex samples, although free CIII particles exhibit varying fractions depending on the detergent used (50). Furthermore, the proportion of free CIII in vesicles matches that observed via BN-PAGE for human CIII

(50 to 60%) purified using digitonin, a relatively mild detergent (51). This finding may partially demonstrate the ability of vesicles to maintain the complex organization of native mitochondria and could be further used to study the organizational plasticity of respiratory chain components in mitochondrial membrane environments. Notably, it remains unclear whether these observations reflect the situation in native mitochondria, as the vesicle preparation process may lead to the disassembly of weakly interacting supercomplexes.

The high-resolution cryo-EM map of CIII in vesicles clearly resolved side-chain features and bound ligands (Fig. 4 *F* and *G* and *SI Appendix*, Fig. S6*E*). The transmembrane region, approximately 45 Å, closely matched previously reported structures from native pig heart mitochondria (49) (Fig. 4*F*). However, we observed pronounced heterogeneity in subunit 9, known to mediate intercomplex interactions. Our structure reveals a continuous density bridge connecting monomers across the symmetry axis (*SI Appendix*, Fig. S7*A*), resembling the configuration observed in detergent-isolated mouse heart CIII. This configuration shows two CIII monomers sharing a single subunit 9 (48, 52) rather than the independent subunit 9 arrangement reported for native pig heart mitochondria (49) (*SI Appendix*, Fig. S7*A*).

Similar to the observations in AcrB, we detected numerous lipid-like densities surrounding the transmembrane region of CIII (*SI Appendix*, Fig. S7*B*). However, the weak density intensities precluded definitive lipid identification, suggesting relatively low specific protein–lipid interactions. This finding aligns with previous studies demonstrating that cardiolipin bound to yeast CIII can be functionally replaced with non-native phosphatidylglycerol (52). Within the transmembrane region, we identified substantial nonprotein density (*SI Appendix*, Fig. S7*B*). While some features corresponded to known cofactors and ligands, such as heme, many densities remain unassigned and warrant further investigation. These observations highlight that, despite the availability of numerous high-resolution structures of respiratory chain complexes, significant opportunities remain to elucidate their structural and functional details through alternative approaches. The inherent complexity and dynamic nature of these multisubunit complexes, along with their diverse array of bound ligands, continue to present important challenges for structural characterization.

Discussion

Here, we report a method to study the native structure of membrane proteins using vesicles, which maximally retain their original lipid environment. Using this approach, we determined the structure of AcrB in vesicles, which revealed a symmetric trimer in the LLL state. Compared to previously determined structures of AcrB in detergent (38) and nanoparticles (39), AcrB in vesicles exhibits distinct features in the exterior TMs and the lα helix bridging TM6 and TM7, probably attributed to the native lipids retained in the vesicles. We further optimized this method for mitochondria isolated from pig heart tissue, enabling the identification of endogenous membrane proteins and high-resolution structure determination of mitochondrial CIII. Our structural analyses demonstrate that CIII particles in vesicles either participate in supercomplex formation or exist independently. While conventional approaches to study structures of mitochondrial membrane proteins rely on detergent extraction and purification, and direct in situ cryo-EM of intact mitochondria faces challenges from organelle size, our vesicle-based method enables efficient, native-state structural determination of endogenous membrane proteins. This approach eliminates the need for complex purification while maintaining membrane integrity, providing a practical bridge between biochemical isolation and cellular context.

To determine the high-resolution structures of membrane proteins in vesicles, we combined different strategies and developed a micrograph-based sorting approach to accurately target and isolate high-quality particles for final 3D reconstruction. We successfully applied this strategy to native mitochondrial membranes containing highly heterogeneous protein populations. Despite the dense packing of proteins and complex organization of mitochondrial membranes, our targeted approach achieved remarkable specificity. Using Topaz models trained specifically on ATP synthase and CIII, which constitute approximately 24.6% and 8.7% (mass fraction) of inner membrane proteins, respectively, we selectively identified particles under native conditions (53). Notably, 2D class averages confirmed precise centering at template-defined positions, with a complete absence of features from other respiratory complexes. This performance demonstrates the robustness of our pipeline for endogenous membrane proteins at high-to-medium abundance levels, overcoming interference from the crowded membrane environment. This approach can also be applied to other cases where target proteins are obscured by strong background noise, such as in vesicles, proteoliposomes, and native biological membranes. The micrograph-based sorting method is also suitable for micrograph and particle classification from cryogrids with nonuniform particle distributions in quantity or quality. Notably, while we can identify some AcrB particles in top and bottom views, the 2D averages do not appear promising compared to the side-view particles, likely due to the severe background noise caused by the two layers of the vesicle membrane. However, we successfully achieved final 3D reconstructions at near-atomic resolution without orientation problems, using only the side-view particles from various angles.

All targeted proteins validated using the vesicle-based methodology exceeded 200 kDa in size, significantly facilitated data processing, particularly in particle picking, classification, and the early stages of 3D reconstruction. To assess the size limitations of our method, we performed symmetry expansion and subtraction on AcrB. As expected, reducing size from trimeric to monomeric AcrB led to a resolution drop when using the same number of particles (*SI Appendix*, Fig. S8 *A* and *B*). Increasing the particle count partially compensated for the resolution loss in monomeric AcrB (*SI Appendix*, Fig. S8*A*). We further divided AcrB into transmembrane and soluble regions, both of which exhibited similar behavior to monomeric and dimeric AcrB (*SI Appendix*, Fig. S8 *A* and *C*). Notably, for subtracted particles, we relied on coordinate information and performed only local refinement. These observations indicate that vesicle-embedded particles align and reconstruct comparably to detergent-solubilized samples in terms of protein size, with resolution improvement achieved through particle population scaling, as shown in previous studies (54, 55). In addition, ResLog analysis revealed no significant differences in the low-resolution region (>4.5 Å) (*SI Appendix*, Fig. S8*A*). We hypothesize that membrane signals from the vesicles likely contribute to and may even predominantly drive, particle alignment at low resolutions, resulting in consistent alignment efficiency across particles of varying sizes. This hypothesis is supported by previous work showing that membrane-derived angular information, through correlated Euler angles between liposome membranes and embedded proteins, enables successful alignment of small protein particles, a task particularly challenging for detergent-solubilized samples (56, 57). However, in the high-resolution region, smaller particles clearly require substantially more particles to achieve comparable

reconstruction quality. This particle quantity requirement escalates further with increasing resolution and decreasing molecular weight. While our methodology enables structural studies of endogenous membrane proteins in native membrane environments, successful implementation depends strongly on both target abundance and particle size. To broaden the applicability of this method, the development of more sophisticated computational approaches will be essential. Size-augmentation strategies (58) used in conventional single-particle analysis could theoretically be adapted for vesicle-embedded targets, though practical implementation presents significant challenges. Looking ahead, we anticipate that integrating advanced deep learning architectures with 3D structural prediction-guided algorithms will dramatically improve the identification and structural determination of challenging targets, particularly for small, low-abundance membrane proteins within complex native membranes.

In the data processing, we noted that the average number of contributing particles of AcrB from each micrograph is quite low compared to purified samples. Although collecting a huge dataset could be helpful, a more efficient strategy is to enrich vesicles containing the target protein in the cryogrids for single-particle cryo-EM data collection. This can be achieved by adding additional protein binding partners during vesicle preparation, such as specific Fabs of target proteins, or during cryosample preparation, such as affinity grids mentioned below (Fig. 5*A*). Currently, the cryo-EM sample preparation of vesicles containing AcrB does not require affinity tags, which is valuable for studying endogenous membrane proteins without modifications to their protein sequences, as demonstrated with CIII from mitochondria. Notably, adding an affinity tag may affect the expression of certain membrane proteins. Further optimization of this method would expand its application in structural and biochemical studies of membrane proteins without the use of detergents.

For a long time, structural studies of integral membrane proteins heavily relied on their solubilization by detergents. Undoubtedly, these structures have advanced our understanding of the working mechanism of the target membrane proteins. To investigate the influence of the lipid environment on membrane proteins, many strategies, including nanodiscs, have been developed to mimic the native lipid context. In this study, we move forward by introducing a vesicle-based method to facilitate structure determination of membrane proteins in their native membrane environment. With further optimization, this method could be widely used to capture the native state of target membrane proteins and may provide important findings.

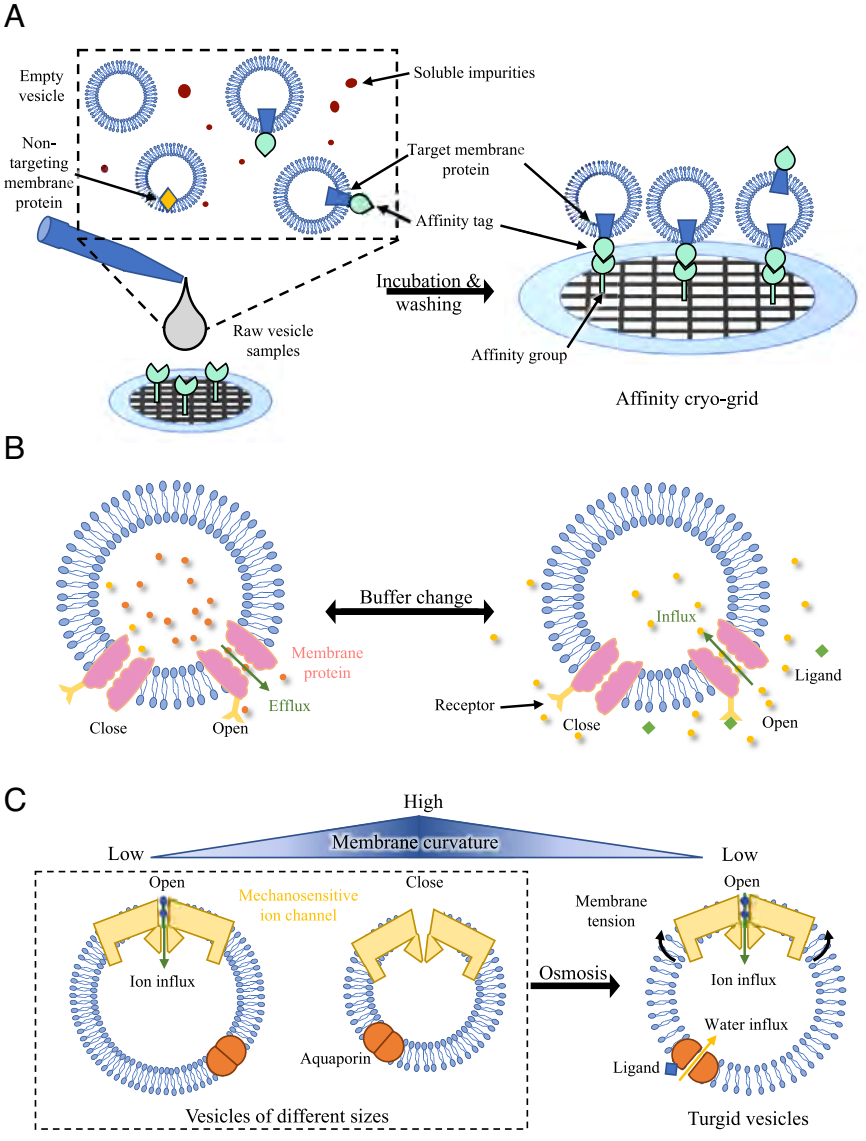

Fig. 5. The potential application of the vesicle-based method. (*A*) Schematics of the vesicle-based method combined with affinity cryogrids for structural studies of membrane proteins. (*B*) Study of membrane proteins under different conditions by changing buffer conditions inside/outside the closed vesicle system. (*C*) Study of mechanical sensor proteins (exemplified by the PIEZO channel) by preparing vesicles of different sizes.

A previous study reported a similar approach by determining the structure of human Slo1, a calcium-activated potassium channel, in vesicles derived from the total cell membrane or plasma membrane of HKE293 GnTI$^-$ cells, where Slo1 was overexpressed (21). Our method, using various membrane-derived vesicles, is a supplement for structure determination of membrane proteins overexpressed in bacteria. We also tested the applicability of our method in mammalian cells, a better recombinant expression system for eukaryotic membrane proteins. We overexpressed TRPV2 in HEK293s GnTI$^-$ cells and prepared vesicles following a similar protocol (*SI Appendix*, Fig. S9*A*). Although we achieved specific picking and 3D classification of TRPV2 particles, we only obtained a medium-resolution structure (*SI Appendix*, Fig. S9 *B* and *C*). Subsequent work will focus on improving the resolution of TRPV2 in vesicles and expanding the application of this method in mammalian expression systems by testing other membrane proteins. Notably, our method does not rely on affinity tags for vesicle preparation, allowing for the study of endogenous membrane proteins in their native cellular context, as demonstrated in mitochondria resident membrane proteins. This is particularly significant, as affinity tags can sometimes interfere with the expression and folding of target membrane proteins.

Compared to methods, like nanodiscs, the vesicle-based method provides a relatively closed system. Additionally, the protein orientation in the vesicle membrane can be changed to be similar or opposite to its native orientation. In the vesicle preparation, the buffer condition inside or outside could be altered as needed, which would provide an opportunity to study target protein under various cellular stimuli (e.g., pH or different ion concentrations). For example, the conformations of some lysosome proteins are directly regulated by pH (59, 60). Our method could provide a strategy to study the pH-mediated conformational changes of such proteins (Fig. 5*B*). In contrast to the proteoliposome system, the vesicle-based method provides a membrane environment that is more similar to the cell membrane environment in which the target membrane proteins naturally exist. The native lipid composition may stabilize protein in a physiologically relevant state and enable us to study the regulatory mechanism of the target membrane protein by some lipids.

Cryo-ET has emerged as a powerful technique for in situ structural studies of proteins and protein complexes in their native states (61–63). By combining cryo-focused ion beam milling with subtomogram averaging, this approach has demonstrated the potential to achieve near-atomic resolution (64, 65). However, cellular complexity and persistent technical challenges in preparing high-quality samples have hindered routine high-resolution structural determination using this approach. Our vesicle-based method overcomes these limitations by providing membrane protein samples ideally sized for single-particle analysis, while maintaining native membrane environments. This approach serves as a valuable alternative for high-resolution in situ structural studies of membrane proteins across diverse biological membranes.

The size of the vesicles could be adjusted during preparation. Larger vesicles have a relatively flattened membrane surrounding the target proteins, while smaller vesicles will cause the membrane surrounding target proteins to bend sharply, generating different membrane forces (Fig. 5*C*). Previous studies have suggested that the transduction of mechanical forces through mechanical sensor proteins is mediated by membrane bending (66). The vesicle-based method can be used to study how mechanical sensor proteins respond to forces of varying magnitudes generated by membrane bending. Furthermore, water and ion channels can be coexpressed with target proteins for vesicle generation, and the activation of these channels can create different osmotic pressure or ion strength prior to cryo-sample freezing to capture various states of the target membrane protein under various conditions (Fig. 5*C*).

In combination with affinity grids based on graphene (67) or graphene oxide (68, 69), our method provides a unique approach to the structural determination of membrane proteins in their native environment without detergent solubilization (Fig. 5*A*). Using this approach, vesicles containing target proteins can be enriched on grids for cryo-EM imaging and data collection. The purification process and sample preparation will be dramatically simplified, with improved efficiency, enabling the capture of weak binding partners and the study of the interaction network of the target membrane proteins.

Materials and Methods

Generation and Purification of Vesicles. Full-length AcrB with N-terminal His tag was overexpressed in *E. coli* BL21(DE3) strain by adding 0.5 mM isopropyl-β-D-thiogalactoside (IPTG) for 16 h at 20 °C when the OD_{600} reached 0.8. The cells were harvested and resuspended in lysis buffers containing 25 mM Tris-HCl (pH 7.5), 150 mM NaCl, and 2 mM $MgCl_2$. After 2 h incubation with lysozyme (5 μg/mL) at 4 °C, the cells were disrupted using a high-pressure homogenizer (French press) at 800 bar for three cycles. The cell pellet was removed by centrifugation at 6,000 g for 30 min. Vesicles were collected by ultracentrifugation at 100,000 g for 30 min. The vesicle pellet was washed twice, resuspended in 30 mL of buffer, homogenized using a high-pressure homogenizer at 1,200 bar for three cycles, and filtered through a 0.42 μm Millipore membrane filter.

Density Gradient Centrifugation of the AcrB Vesicles. To further purify the vesicles, we employed two types of sucrose density gradient centrifugation methods, considering the various experimental requirements and hardware conditions of the labs (*SI Appendix*, Fig. S1).

For the vesicle quality analysis and accurate purification, a continuous sucrose density gradient was applied to the samples (*SI Appendix*, Fig. S1*A*). A 9 mL 30% (W/V) sucrose solution in lysis buffer was added to a 10 mL ultraspeed centrifugation tube and slowly freeze-thawed for three cycles between −20 °C and 4 °C to generate a smooth sucrose density gradient from 25 to 35% (70). A 1 mL concentrated vesicle sample was added to the top and centrifuged at 50,000 g for 14 h. Twenty fractions were manually aspirated using a pipette, and the protein concentration and purity of each fraction were assessed using the UV280 absorption and SDS-PAGE.

For faster purification and higher final vesicle concentration, a noncontinuous sucrose density gradient was applied (*SI Appendix*, Fig. S1*B*). A 3 mL 40% (W/V) sucrose and a 2 mL 20% sucrose in the lysis buffer were added to a 10 mL ultraspeed centrifugation tube, and 5 mL of the vesicle sample was carefully layered on top. The solution was centrifuged at 10,0000 g for 45 min. The vesicle fractions, concentrated between the 20% and 40% sucrose layers (*SI Appendix*, Fig. S1*C*), were gently collected from the tube based on the position of the yellow band.

For negative stain and cryo-EM grids preparation, the fractions were repeatedly diluted with no-sucrose lysis buffer and concentrated using a 100 kD Amicon centrifugal filter to decrease the sucrose concentration to below 1%. The final samples were concentrated to around 2 mg/mL for cryo-EM grid preparation.

Generation and Purification of Mitochondrial Vesicles. Mitochondria were purified from pig heart muscle cells primarily following modified classical protocols (51). Briefly, a pig heart (slaughtered 4 h prior) was washed with a buffer containing 250 mM sucrose, 10 mM Tris-HCl (pH 7.8), and 0.2 mM EDTA. The heart muscle was then cut into 1 to 2 cm cubes with the removal of any nonmuscle tissues. The muscle pieces were washed and cooled to 4 °C in 450 mL of buffer supplemented with protease inhibitors (0.3 μM Aprotinin, 0.3 μM Pepstatin, 3 μM Leupeptin) for homogenization using a blender until the lysate was free of visible particulates with a stable pH.

After centrifugation at 750 g for 10 min, the supernatant was subjected to another centrifugation at 4,500 g for 35 min to collect the mitochondria. The pellet was resuspended and centrifuged at 9,000 g for 10 min to wash the mitochondria. The final pellet was resuspended in 45 mL of buffer containing 25 mM Tris-HCl and 150 mM NaCl, with the addition of 0.2 mM EDTA and protease inhibitors (1 μM Aprotinin, 1 μM Pepstatin, 10 μM Leupeptin). The mitochondrial vesicles were prepared using a strategy similar for the bacterial vesicle. The vesicle samples were concentrated to approximately 2 mg/mL for cryosample preparation without density centrifugation.

Negative Staining. 3 μL of samples were loaded onto a glow-discharged formvar, carbon-coated copper grid (300 mesh, Zhongjingkeyi Technology) and incubated for 45 s. The grids were blotted with filter paper and washed with the 2% (w/v) uranyl acetate. Subsequently, the grids were negatively stained with 2% (w/v) uranyl acetate for 45 s and dried with filter paper. The prepared grids were observed and imaged using a Talos L120C electron microscope (Thermo Fisher Scientific) operated at 120 kV, equipped with a 4 k × 4 k Ceta 16 M camera. Images were captured at a magnification of 57,000×, corresponding to a pixel size of 2.49 Å on the specimen, with a defocus of around −1.5 μm.

Cryo-EM Sample Preparation and Data Collection. Following negative staining results to assess sample quality, uniform purified vesicle samples with high contrast were applied to cryogrids. Several trials indicated that the vesicles from *E. coli* demonstrated a strong preference for carbon film over the holes in holey carbon grids (*SI Appendix*, Fig. S1*D*). Therefore, the high-concentration sample was necessary for high-quality grid preparation.

Briefly, 3 μL of vesicle samples from the previous step were loaded to glow-discharged Au holey carbon grids (C-flat, 300 mesh, R1.2/1.3) using a Vitrobot Mark IV (Thermo Fisher Scientific) for 45 s at 100% humidity and 4 °C. Then, the grids were blotted with a blot force of 0 for 3.5 s and plunge-frozen into liquid ethane cooled by liquid nitrogen.

The cryogrids were imaged using a 300 kV Titan Krios G3i electron microscope (Thermo Fisher Scientific) equipped with a K3 Summit direct electron detector (Gatan). For single particle data, automatic data collection was performed using EPU with a 20-eV slit width of the Gatan Imaging Filter (GIF) Bio Quantum in counting mode. Each movie contained 40 frames with a total dose of 50 $e^-/Å^2$ for a 3.74-s exposure time. The pixel size was 1.06 Å. For the tomography data, automatic data collection was performed using Tomography (Thermo Fisher Scientific). The tilt series was captured between −60° and 60° with a 3° step under the dose-symmetry mode. The tilt movie at every angle contained 5 frames at a calibrated pixel size of 2.669 Å/pix with a total dose of 2.976 $e^-/Å^2$. The defocus was set to −3 μm.

Cryo-EM Single Particle Data Processing of AcrB. The main steps of data processing were performed in cryoSPARC (33) (*SI Appendix*, Fig. S3 *A*–*C*). To accurately pick more particles from the vesicles, multiple strategies were used and combined (*SI Appendix*, Fig. S3*A*). Finally, 91,412 particles were harvested, and one class comprising 31,523 particles from ab initio reconstruction was directly aligned by Local refinement (71). This process yielded middle-resolution results for AcrB in vesicles, achieving a structure resolution of 7.5 Å. Our micrograph-based sorting method was applied to further enrich the particles and improve the accuracy of 3D refinement (*SI Appendix*, Fig. S3*B*). We selected all micrographs containing more than 20 particles, resulting in a total of 5,554 particles and 226 micrographs for Topaz (34, 35) training. The well-trained model was then applied to 1,068 micrographs, each with a previous particle count exceeding 10, yielding a 6.5-Å map using 24,191 particles after 2D and 3D classification. Finally, Topaz picked 1,560,821 particles from all other images, from which 666,048 particles were selected for further processing. In the final step, 3D seed-guided 3D classification separated 100,536 high-quality particles, pushing the resolution to 5.8 Å (*SI Appendix*, Fig. S3*C*). The multiclass ab initio reconstruction and heterogeneous refinement were employed to sort out 75,150 good particles. Local refinement, masking only the protein region, resolved the structure at 4.53 Å with C3 symmetry. After 5 iterations of CryoSieve (36), 24,537 particles remained, yielding a cryo-EM map of AcrB in vesicles at 4.1 Å, achieved through Local refinement. These particles and maps were used as seeds for another round of 3D classification, followed by 5 iterations of CryoSieve (36). This process generated the final cryo-EM map at 3.88 Å using Local refinement with 49,252 particles. The map was postprocessed with DeepEMhancer (72) using the highRes model. Structural comparisons and image rendering were conducted using UCSF Chimera (73) and ChimeraX (74). Additional details can be found in *SI Appendix*, Fig. S3.

Cryo-EM Single Particle Data Processing of Complex III (CIII). The data processing workflow for CIII closely followed the protocols used for the AcrB vesicle dataset and was mainly performed in cryoSPARC (33) (*SI Appendix*, Fig. S6 *A* and *B*). To improve processing speed and reduce file size, a subset of 1,855 images was selected for preliminary analysis (*SI Appendix*, Fig. S6*A*). The 2D projections of the vesicle membranes served as initial templates for particle picking. After four rounds of 2D classification, two predominant protein features emerged, identified as F-ATPase and CIII. The 2D projections of these proteins were then employed as templates for subsequent particle picking. Additionally, our micrograph-based sorting method was applied to facilitate data processing by sorting out higher-quality particles. These particle datasets were further utilized to train the Topaz model and pick more particles. The sorting and training process was repeated to obtain two well-trained Topaz models for specifically and efficiently selecting F-ATPase and CIII from mitochondrial membrane vesicles. For CIII, 104,570 good particles from heterogeneous refinement were selected to reconstruct a cryo-EM density map at 3.46 Å using nonuniform refinement. Following CTF refinement and local refinement, CryoSieve (36) was employed to further push resolution to 3.0 Å with 42,832 particles. The map was postprocessed with DeepEMhancer (72) using the highRes model. Structural comparisons and image rendering were conducted using UCSF Chimera (73) and ChimeraX (74).

Cryo-EM Tomography Data Processing. Motion correction was automatically finished by Tomography (Thermo Fisher Scientific) without the dose weighting. The tilt series were subsequently transferred into Etomo (75) of IMOD for image alignment and tomogram reconstruction. CTF parameters were manually estimated using Ctfplotter (76, 77). The final tomograms were processed in bin 3 to reduce the file size, and gold particles were erased to minimize signal interference. The tomograms were then denoised using IsoNet (78) to improve contrast. The Segmentation of EMAN2 (79, 80), a convolutional neural network based tool, was employed to locate the membrane density of vesicles in the denoised tomograms and generate 3D volumes of vesicle distribution. The image rendering was conducted using 3dmod of IMOD and UCSF ChimeraX.

Data, Materials, and Software Availability. Cryo-EM density maps of AcrB and respiratory complex III in vesicles have been deposited in the Electron Microscopy Data Bank with accession no. EMD-62301 and EMD-63981 (81, 82), respectively.

ACKNOWLEDGMENTS. All cryo-EM data were collected at the Biological cryo-electron microscopy (cryo-EM) Center at the Hong Kong University of Science and Technology (HKUST), generously supported by a donation from the Lo Kwee Seong Foundation. This project is supported by grants from the Hong Kong Research Grants Council (GRF16103321, GRF16102822, GRF16100223, C5033-19E, C6001-21E, and C6012-22G), Shenzhen Special Fund for Local Science and Technology Development Guided by Central Government (2021Szvup140), HKUST VPRDO 30-for-30 Research Initiative Scheme, and HKUST start-up and initiation grants.

1. M. Rask-Andersen, M. S. Almén, H. B. Schiöth, Trends in the exploitation of novel drug targets. *Nat. Rev. Drug Discov.* **10**, 579–590 (2011).
2. L. Tiefenauer, S. Demarche, Challenges in the development of functional assays of membrane proteins. *Materials* **5**, 2205–2242 (2012).
3. J. Deisenhofer, O. Epp, K. Miki, R. Huber, H. Michel, Structure of the protein subunits in the photosynthetic reaction centre of Rhodopseudomonas viridis at 3 resolution. *Nature* **318**, 618–624 (1985).
4. D. Kozma, I. Simon, G. E. Tusnády, PDBTM: Protein data bank of transmembrane proteins after 8 years. *Nucleic Acids Res.* **41**, D524–D529 (2013).
5. V. Kotov *et al.*, High-throughput stability screening for detergent-solubilized membrane proteins. *Sci. Rep.* **9**, 1–19 (2019).
6. A. Anandan, A. Vrielink, Detergents inmembrane protein purification and crystallisation. *Adv. Exp. Med. Biol.* **922**, 13–28 (2016).
7. P. Champeil *et al.*, A robust method to screen detergents for membrane protein stabilization, revisited. *Anal. Biochem.* **511**, 31–35 (2016).
8. G. Lenoir *et al.*, Screening of detergents for stabilization of functional membrane proteins. *Curr. Protoc. Protein Sci.* **93**, e59 (2018).
9. T. Arnold, D. Linke, The use of detergents to purify membrane proteins. *Curr. Protoc. Protein Sci.* 4.8.1–4.8.30 (2008), 10.1002/0471140864.ps0408s53.
10. J. A. Lundbæk, S. A. Collingwood, H. I. Ingólfsson, R. Kapoor, O. S. Andersen, Lipid bilayer regulation of membrane protein function: Gramicidin channels as molecular force probes. *J. R. Soc. Interface* **7**, 373–395 (2010).

11. Z. Yuan, S. B. Hansen, Cholesterol regulation of membrane proteins revealed by two-color super-resolution imaging. *Membranes* **13**, 250 (2023).
12. I. Levental, E. Lyman, Regulation of membrane protein structure and function by their lipid nano-environment. *Nat. Rev. Mol. Cell Biol.* **24**, 107–122 (2023).
13. H. E. Autzen, D. Julius, Y. Cheng, Membrane mimetic systems in cryoEM: Keeping membrane proteins in their native environment. *Curr. Opin. Struct. Biol.* **58**, 259–268 (2019).
14. I. G. Denisov, S. G. Sligar, Nanodiscs for structural and functional studies of membrane proteins. *Nat. Struct. Mol. Biol.* **23**, 481–486 (2016).
15. J. M. Pettersen, Y. Yang, A. S. Robinson, Advances in nanodisc platforms for membrane protein purification. *Trends Biotechnol.* **41**, 1041–1054 (2023).
16. J. Frauenfeld *et al.*, A saposin-lipoprotein nanoparticle system for membrane proteins. *Nat. Methods* **13**, 345–351 (2016).
17. M. Jamshad *et al.*, Surfactant-free purification of membrane proteins with intact native membrane environment. *Biochem. Soc. Trans.* **39**, 813–818 (2011),
18. X. Yang *et al.*, Structure deformation and curvature sensing of PIEZO1 in lipid membranes. *Nature* **604**, 377–383 (2022).
19. X. Yao, X. Fan, N. Yan, Cryo-EM analysis of a membrane protein embedded in the liposome. *Proc. Natl. Acad. Sci. U.S.A.* **117**, 18497–18503 (2020).
20. L. Tonggu, L. Wang, Broken symmetry in the human BK channel. *SSRN Electron. J.*, 494385 (2019), 10.2139/ssrn.3310822.
21. X. Tao, C. Zhao, R. MacKinnon, Membrane protein isolation and structure determination in cell-derived membrane vesicles. *Proc. Natl. Acad. Sci. U.S.A.* **120**, e2302325120 (2023).
22. C. Wang *et al.*, Structure and topography of the synaptic V-ATPase–synaptophysin complex. *Nature* **631**, 899–904 (2024).
23. C. E. Coupland *et al.*, High-resolution electron cryomicroscopy of V-ATPase in native synaptic vesicles. *Science* **385**, 168–174 (2024).
24. Y. Matsunaga *et al.*, Energetics and conformational pathways of functional rotation in the multidrug transporter AcrB. *Elife* **7**, e31715 (2018).
25. T. Eicher *et al.*, Transport of drugs by the multidrug transporter AcrB involves an access and a deep binding pocket that are separated by a switch-loop. *Proc. Natl. Acad. Sci. U.S.A.* **109**, 5687–5692 (2012).
26. G. P. Gorbenko, V. M. Ioffe, P. K. J. Kinnunen, Binding of lysozyme to phospholipid bilayers: Evidence for protein aggregation upon membrane association. *Biophys. J.* **93**, 140–153 (2007).
27. H. R. Ibrahim *et al.*, Partially unfolded lysozyme at neutral pH agglutinates and kills gram-negative and gram-positive bacteria through membrane damage mechanism. *J. Agric. Food Chem.* **44**, 3799–3806 (1996).
28. N. Nawaz *et al.*, Lysozyme and its application as antibacterial agent in food industry. *Molecules* **27**, 6305 (2022).
29. M. Derde *et al.*, Hen egg white lysozyme permeabilizes Escherichia coli outer and inner membranes. *J. Agric. Food Chem.* **61**, 9922–9929 (2013).
30. A. Pellegrini *et al.*, Identification and isolation of a bactericidal domain chicken egg white lysozyme. *J. Appl. Microbiol.* **82**, 372–378 (1997).
31. Y. Liu, F. J. Sigworth, Automatic cryo-EM particle selection for membrane proteins in spherical liposomes. *J. Struct. Biol.* **185**, 295–302 (2014).
32. Q. X. Jiang, D. W. Chester, F. J. Sigworth, Spherical reconstruction: A method for structure determination of membrane proteins from cryo-EM images. *J. Struct. Biol.* **133**, 119–131 (2001).
33. A. Punjani, J. L. Rubinstein, D. J. Fleet, M. A. Brubaker, CryoSPARC: Algorithms for rapid unsupervised cryo-EM structure determination. *Nat. Methods* **14**, 290–296 (2017).
34. T. Bepler *et al.*, Positive-unlabeled convolutional neural networks for particle picking in cryo-electron micrographs. *Nat. Methods* **16**, 1153–1160 (2019).
35. T. Bepler, K. Kelley, A. J. Noble, B. Berger, Topaz-denoise: General deep denoising models for cryoEM and cryoET. *Nat. Commun.* **11**, 1–12 (2020).
36. J. Zhu *et al.*, A minority of final stacks yields superior amplitude in single-particle cryo-EM. *Nat. Commun.* **14**, 1–11 (2023).
37. J. Kobylka, M. S. Kuth, R. T. Müller, E. R. Geertsma, K. M. Pos, AcrB: A mean, keen, drug efflux machine. *Ann. N. Y. Acad. Sci.* **1459**, 38–68 (2020).
38. S. Murakami, R. Nakashima, E. Yamashita, A. Yamaguchi, Crystal structure of bacterial multidrug efflux transporter AcrB. *Nature* **419**, 587–593 (2002).
39. W. Qiu *et al.*, Structure and activity of lipid bilayer within a membrane-protein transporter. *Proc. Natl. Acad. Sci. U.S.A.* **115**, 12985–12990 (2018).
40. S. Murakami, R. Nakashima, E. Yamashita, T. Matsumoto, A. Yamaguchi, Crystal structures of a multidrug transporter reveal a functionally rotating mechanism. *Nature* **443**, 173–179 (2006).
41. H. Cha, K. M. Pos, "Transport mechanism and proton-coupling in the multidrug efflux transporter complex ArcAB-TolC" in *Springer Series in Biophysics*, R. Krämer, C. Ziegler, Eds. (Springer, Berlin, Heidelberg, 2014), vol. 17, pp. 207–232.
42. Y. Gao, E. Cao, D. Julius, Y. Cheng, TRPV1 structures in nanodiscs reveal mechanisms of ligand and lipid action. *Nature* **534**, 347–351 (2016).
43. M. Zwama, A. Yamaguchi, Molecular mechanisms of AcrB-mediated multidrug export. *Res. Microbiol.* **169**, 372–383 (2018).
44. C. Gerle *et al.*, Human F-ATP synthase as a drug target. *Pharmacol. Res.* **209**, 107423 (2024).
45. J. Gu *et al.*, Cryo-EM structure of the mammalian ATP synthase tetramer bound with inhibitory protein IF1. *Science* **364**, 1068–1075 (2019).
46. T. B. Blum, A. Hahn, T. Meier, K. M. Davies, W. Kühlbrandt, Dimers of mitochondrial ATP synthase induce membrane curvature and self-assemble into rows. *Proc. Natl. Acad. Sci. U.S.A.* **116**, 4250–4255 (2019).
47. J. M. Di Trani *et al.*, Cryo-EM of native membranes reveals an intimate connection between the Krebs cycle and aerobic respiration in mycobacteria. *Proc. Natl. Acad. Sci. U.S.A.* **122**, e2423761122 (2025).
48. I. Vercellino, L. A. Sazanov, Structure and assembly of the mammalian mitochondrial supercomplex CIII2CIV. *Nature* **598**, 364–367 (2021).
49. W. Zheng, P. Chai, J. Zhu, K. Zhang, High-resolution in situ structures of mammalian respiratory supercomplexes. *Nature* **631**, 232–239 (2024).
50. R. Acín-Pérez, P. Fernández-Silva, M. L. Peleato, A. Pérez-Martos, J. A. Enriquez, Respiratory active mitochondrial supercomplexes. *Mol. Cell* **32**, 529–539 (2008).
51. T. Lobo-Jarne, C. Ugalde, Respiratory chain supercomplexes: Structures, function and biogenesis. *Semin. Cell Dev. Biol.* **76**, 179–190 (2018).
52. C. F. Hryc *et al.*, Structural insights into cardiolipin replacement by phosphatidylglycerol in a cardiolipin-lacking yeast respiratory supercomplex. *Nat. Commun.* **14**, 1–13 (2023).
53. M. Schlame, Protein crowding in the inner mitochondrial membrane. *Biochim. Biophys. Acta* **1862**, 148305 (2021).
54. X. Fan *et al.*, Single particle cryo-EM reconstruction of 52 kDa streptavidin at 3.2 angstrom resolution. *Nat. Commun.* **10**, 1–11 (2019).
55. Y. Xu *et al.*, Metallo-supramolecular branched polymer protects particles from air-water interface in single-particle cryo-electron microscopy. *Commun. Biol.* **7**, 1–10 (2024).
56. L. Wang, F. J. Sigworth, "Liposomes on a streptavidin crystal. A system to study membrane proteins by cryo-EM" in *Cryo-EM Part A Sample Preparation and Data Collection*, G. J. Jensen, Ed. (*Methods in Enzymology*, Academic Press, 2010), vol. 481, pp. 147–164.
57. L. Wang, F. J. Sigworth, Structure of the BK potassium channel in a lipid membrane from electron cryomicroscopy. *Nature* **461**, 292–295 (2009).
58. K. Wentinck, C. Gogou, D. H. Meijer, Putting on molecular weight: Enabling cryo-EM structure determination of sub-100-kDa proteins. *Curr. Res. Struct. Biol.* **4**, 332–337 (2022).
59. R. Wang, X. Qi, P. Schmiege, E. Coutavas, X. Li, Marked structural rearrangement of mannose 6-phosphate/IGF2 receptor at different pH environments. *Sci. Adv.* **6**, eaaz1466 (2020).
60. X. Guo *et al.*, Structure and mechanism of human cystine exporter cystinosin. *Cell* **185**, 3739–3752. e18 (2022).
61. W. Wan, J. A. G. Briggs, "Cryo-electron tomography and subtomogram averaging" in *The Resolution Revolution: Recent Advances in cryoEM*, R. A. Crowther, Ed. (*Methods in Enzymology*, Academic Press, 2016), vol. 579, pp. 329–367.
62. O. Medalia *et al.*, Macromolecular architecture in eukaryotic cells visualized by cryoelectron tomography. *Science* **298**, 1209–1213 (2002).
63. A. Doerr, Cryo-electron tomography. *Nat. Methods* **14**, 34 (2016).
64. Z. Wang *et al.*, Structures from intact myofibrils reveal mechanism of thin filament regulation through nebulin. *Science* **375**, eabn1934 (2022).
65. C. Berger *et al.*, Cryo-electron tomography on focused ion beam lamellae transforms structural cell biology. *Nat. Methods* **20**, 499–511 (2023).
66. A. H. Lewis, J. Grandl, Mechanical sensitivity of Piezo1 ion channels can be tuned by cellular membrane tension. *Elife* **4**, e12088 (2015).
67. N. Liu *et al.*, Bioactive functionalized monolayer graphene for high-resolution cryo-electron microscopy. *J. Am. Chem. Soc.* **141**, 4016–4025 (2019).
68. F. Wang *et al.*, General and robust covalently linked graphene oxide affinity grids for high-resolution cryo-EM. *Proc. Natl. Acad. Sci. U.S.A.* **117**, 24269–24273 (2020).
69. F. Wang *et al.*, Amino and PEG-amino graphene oxide grids enrich and protect samples for high-resolution single particle cryo-electron microscopy. *J. Struct. Biol.* **209**, 107437 (2020).
70. K. L. Baxter-Gabbard, A simple method for the large-scale preparation of sucrose gradients. *FEBS Lett.* **20**, 117–119 (1972).
71. A. Punjani, H. Zhang, D. J. Fleet, Non-uniform refinement: Adaptive regularization improves single-particle cryo-EM reconstruction. *Nat. Methods* **17**, 1214–1221 (2020).
72. R. Sanchez-Garcia *et al.*, DeepEMhancer: A deep learning solution for cryo-EM volume post-processing. *Commun. Biol.* **4**, 1–8 (2021).
73. E. F. Pettersen *et al.*, UCSF chimera–A visualization system for exploratory research and analysis. *J. Comput. Chem.* **25**, 1605–1612 (2004).
74. T. D. Goddard *et al.*, UCSF chimeraX: Meeting modern challenges in visualization and analysis. *Protein Sci.* **27**, 14–25 (2018).
75. J. R. Kremer, D. N. Mastronarde, J. R. McIntosh, Computer visualization of three-dimensional image data using IMOD. *J. Struct. Biol.* **116**, 71–76 (1996).
76. Q. Xiong, M. K. Morphew, C. L. Schwartz, A. H. Hoenger, D. N. Mastronarde, CTF determination and correction for low dose tomographic tilt series. *J. Struct. Biol.* **168**, 378–387 (2009).
77. D. N. Mastronarde, Accurate, automatic determination of astigmatism and phase with Ctfplotter in IMOD. *J. Struct. Biol.* **216**, 108057 (2024).
78. Y. T. Liu *et al.*, Isotropic reconstruction for electron tomography with deep learning. *Nat. Commun.* **13**, 1–17 (2022).
79. M. Chen *et al.*, Convolutional neural networks for automated annotation of cellular cryo-electron tomograms. *Nat. Methods* **14**, 983–985 (2017).
80. G. Tang *et al.*, EMAN2: An extensible image processing suite for electron microscopy. *J. Struct. Biol.* **157**, 38–46 (2007).
81. H. Liu, S. Dang, Cryo-EM structure of AcrB in vesicles. Electron Microscopy Data Bank. https://www.ebi.ac.uk/emdb/EMD-62301. Deposited 7 November 2024.
82. H. Liu, S. Dang, Cryo-EM structure of complex III2 of mammalian respiratory supercomplex in vesicles. Electron Microscopy Data Bank. https://www.ebi.ac.uk/emdb/EMD-63981. Deposited 31 March 2025.